

Dual-reference Training Data Acquisition and CNN Construction for Image Super-Resolution

Yanhui Guo, Xiao Shu, and Xiaolin Wu, *Fellow, IEEE*

Abstract—For deep learning methods of image super-resolution, the most critical issue is whether the paired low and high resolution images for training accurately reflect the sampling process of real cameras. Low and high resolution (LR~HR) image pairs synthesized by existing degradation models (*e.g.*, bicubic downsampling) deviate from those in reality; thus the super-resolution CNN trained by these synthesized LR~HR image pairs does not perform well when being applied to real images. In this paper, we propose a novel method to capture a large set of realistic LR~HR image pairs using real cameras. The data acquisition is carried out under controllable lab conditions with minimum human intervention and at high throughput (about 500 image pairs per hour). The high level of automation makes it easy to produce a set of real LR~HR training image pairs for each camera. Our innovation is to shoot images displayed on an ultra-high quality screen at different resolutions. There are three distinctive advantages with our method that allow us to collect high-quality training datasets for image super-resolution. First, as the LR and HR images are taken of a 3D planar surface (the screen) the registration problem fits exactly to a homography model. Second, we can display special markers on the image margin to further improve the registration precision. Third, the displayed digital image file can be exploited as a reference to optimize the high frequency content of the restored image. Experimental results show that training a super-resolution CNN by our LR~HR dataset has superior restoration performance than training it by existing datasets on real world images at the inference stage.

Index Terms—Super resolution, Convolutional neural network, Super-resolution datasets, Dual-reference training data

I. INTRODUCTION

Single image super-resolution (SR), the task of increasing the spatial resolution and details of a given image, has attracted great attention from the computer vision research communities in the last few decades [1]–[7]. In recent years, the state of the art of SR has been set and reset by various deep convolutional neural network (DCNN) based techniques [8]–[12]. In addition to the significant improvement in SR performance, these DCNN techniques also provide some important insights on the designs of DCNN architectures [13]–[20] and loss functions [21]–[24]. However, for any real-world problems, the efficacy of a machine learning technique relies not only on the design of the technique itself but also, sometimes even more critically, on the quality and representativeness of the training data.

As it is impossible to have real LR~HR image pairs, most existing SR techniques resort to synthetically generated low-resolution (LR) images for training. The overly-simplistic downsampling operators commonly employed by these techniques, such as bicubic downsampling (BD) and Gaussian downsampling (GD), cannot accurately simulate the complex and compounded process of capturing a low-resolution image. When operating on real images, the DCNNs trained on

these synthesized datasets generally cannot superresolve high frequency details to the same level of clarity and sharpness as when operating on synthetic LR images. This weakness of synthetic training images is well known to practitioners.

It is not easy to replace synthetic images with real ones in the training of SR networks. Capturing perfectly aligned real LR~HR image pairs is a highly challenging and expensive task. There have been a few attempts to collect datasets of paired LR and HR images [25]–[27]. Their basic idea is to capture each natural scene twice with lenses of different scale factors (focal lengths). Then, they form an image pair by aligning the two images using image registration techniques, possibly patch by patch. Although DCNNs trained with existing real datasets exhibit some improvement for certain types of real images, this real image collection approach is inherently problematic. Firstly, since each scene is captured twice, a scene has to be absolutely static between the two shots in order to avoid mismatches of the paired images. Thus, any moving subjects, such as animals or humans, cannot be included in the datasets. The restriction of no motions greatly narrows the scope of the training images. Secondly, registration errors caused by the perspective misalignment as described in Sec III-B and the different defocus blur effects of the two lenses could also lead to mismatches of LR and HR image pairs. These mismatches due to disparity are inevitable in scenes of depth variations. Thirdly, the resolution difference of LR and HR images also limits the registration accuracy. The lack of alignment precision between LR and HR training images can throw off the deep learning process, hindering the reconstruction of sharp image details.

Except the aforementioned difficulties of the real SR datasets collection, another thorny issue is that the real SR datasets are not camera-agnostic. This problem is caused by variant specifications (*e.g.* pixel pitch, noise model, sensitivity and *etc.*) of different camera sensors. These different factors could make the collected LR images obey a specific distribution which is highly dependent on the camera used for shooting. The SR DCNN trained with this camera-specific dataset thus inclines to overfit the camera and performs poorly outside the dataset. One simple way is to collect a large number of image pairs using all cameras for which the SR DCNN is designed. However, this is not practical, because collecting the diverse large dataset by shooting many scenes using different cameras is laborious and time consuming. Moreover, the SR DCNN trained by the mixed dataset will not yield the best results for a specific camera.

To circumvent the above difficulties, we propose a novel concept of SR training dataset of monitor-induced dual-reference paired images (MIDPI). The LR images X_i for

training the SR network are real, physically acquired ones, rather than some algorithmically downsampled version of the corresponding HR image Y_i (digital image file). The HR image Y_i is displayed on an ultra-high resolution high-quality monitor; this displayed image is captured twice by a camera, in high resolution via a long focal lens, and also in low resolution via a short focal lens, generating the captured HR image \hat{Y}_i and LR image X_i respectively. The (X_i, \hat{Y}_i) image pair provides the deep learning SR network model with the information on pixel PSF, sensor noise statistics, lens characteristics, *etc.* These physical attributes are very difficult to model analytically as they are complex and compounded to each other; their effects on the SR task are best left for a data-driven CNN to factor in.

But the captured HR screen image \hat{Y}_i by itself is not suited to be the ground truth, because it is not an exact copy of the original Y_i . To compensate for this we also include Y_i as a part of the ground truth, and introduce a new learning task of dual-reference SR, using the augmented training image data (X_i, \hat{Y}_i, Y_i) . In other words, the ground truth is now the dual references (\hat{Y}_i, Y_i) . The role of the original HR digital image Y_i is to provide structural information on high frequency features that might be compromised by the analog operation of screen shooting. Fig. 1 illustrates the data collection process of MIDPI.

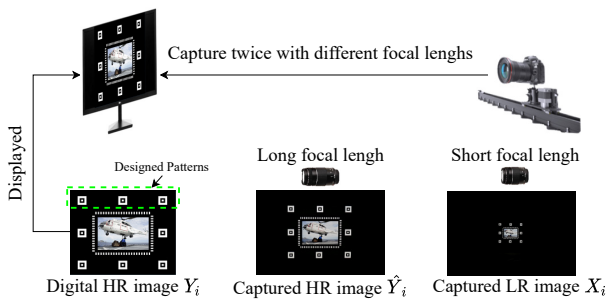


Fig. 1: Illustration of the data collection process of MIDPI.

The proposed process of shooting a ultra-high quality monitor to create paired LR~HR training images has a unique and big advantage over the existing methods of shooting real LR~HR image pairs [26], [27]. That is, the former can achieve a much higher registration accuracy between the captured LR image X_i and the captured HR image \hat{Y}_i ; and in turn, between X_i and Y_i . Indeed, now our registration problem can be modeled exactly by homography transform for the screen image is a 3D planar surface. The flatness of the screen also prevents the problems of occlusion and defocusing due to depth disparity in pairing. In addition, as the scene of the captured image pairs is static, absolutely no object motions exist to cause spatially varying alignment parameters. To push the registration accuracy to the limit, we also display specially designed registration markers on the screen. These markers are used to align LR~HR image pairs to sub-pixel precision by frequency and phase estimation techniques.

The screen shooting is carried out in a controlled dark room lab. environment to eliminate ambient lights. The camera sensor projection plane is calibrated to align with and have sufficient distance from the screen surface to prevent moire

interferences and geometric distortions. Finally, the training image acquisition and pairing process is carefully designed so that even if a small registration error exists, the error will be the same for all LR~HR image pairs. This small constant error in registration will only cause an indiscernible shift of the reconstructed HR image from Y_i , but not blurring artifacts.

Another advantage of the proposed LR~HR image data collection procedure is its scalability to data volume. Once the shooting environment is setup, the whole procedure, including capturing and alignment, can be easily automated without manual intervention. The data collection throughput can reach 500 image pairs per hour. Moreover, the same procedure can be conveniently and quickly repeated for different cameras. This allows the creation of a large training dataset dedicated to a specific camera with ease, opening up the possibility to optimize a SR CNN method for each camera. In contrast, all previous methods of shooting real LR~HR image pairs are highly laborious and very expensive, not scalable to the size of training datasets nor to the number of different cameras.

II. RELATED WORK

There are several popular datasets that have been extensively used for training and testing in SR, such as Set5 [28], Set14 [29], Urban100 [6] and DIV2K [30]. In all of these datasets, the LR images were generated from the HR images via synthetic degradation like bicubic downsampling or Gaussian blurring followed by direct downsampling [31]. Xu *et al.* [32] proposed a method to generate approximate realistic training data by simulating the imaging process of digital cameras. Yoo *et al.* [33] proposed a CutBlur method to augment training data for super-resolution. Jeon *et al.* [34] and Wang *et al.* [35] tried to improve super-resolution performance by using stereo low resolution images. Besides, Generative adversarial networks (GANs) have also been applied to generate realistic degraded images [36]–[38]. Nevertheless, all these synthetic datasets are still far away from the real images.

Recently, some researchers have attempted to capture real-world image pairs for SR. Qu *et al.* [39] obtained paired LR~HR images by placing a beam splitter in the optical path of two identical camera sensors. But their dataset only includes face images. Köhler *et al.* [40] implemented hardware binning on the sensors to collect real data, but it only has 14 scenes. Zhang *et al.* [27] collected 500 scenes using multiple focal lengths. However, they cannot register the paired images precisely because of perspective misalignment. Chen *et al.* [25] printed 100 images to postcards and captured LR~HR image pairs, but the models trained on this dataset cannot generalize well to real-world scenes and they cannot register the image pairs precisely by only using SIFT [41] features. Cai *et al.* [26] collected 595 LR~HR image pairs using two digital single-lens reflex (DSLR) cameras. However, they meet the perspective misalignment as same as [27] and they cannot capture paired data from dynamic scenes. Different from them, our MIDPI system can automatically generate enough precisely aligned LR~HR image pairs at a low cost.



Fig. 2: Illustration of the MIDPI system employed in our experiment.

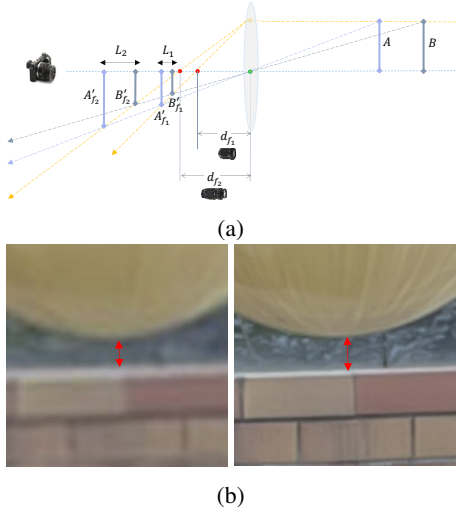


Fig. 3: (a) Illustration of the inherent perspective change between two objects A and B with different depth. d_{f_1} and d_{f_2} represent the focal length for capturing LR images (A'_{f_1} , B'_{f_1}) and HR images (A'_{f_2} , B'_{f_2}) respectively ($d_{f_1} > d_{f_2}$). It is obvious that $\frac{d_{f_2}}{d_{f_1}} \neq \frac{L_2}{L_1}$, which induces the ineludible misalignment when capturing the real paired images in the real world. (b) It shows the perspective misalignment of a paired LR~HR image from Cai *et al.* [26] after registration.

III. METHOD

In this section, we present the details of the proposed procedure of generating SR training datasets of monitor-induced dual-reference paired images (MIDPI).

A. Images capture system

TABLE I: Camera configuration and the number of captured image pairs.

Camera	Sony Nex-6	Canon 5D-MarkIII	Sony Alpha-a7RII
Aperture	f/10	f/10	f/10
Shutter speed	1/30s	1/50s	1/30s
Focal length	18mm&80mm	30mm&120mm	18mm&80mm
Pixel pitch	4.8 μ m	6.2 μ m	6.0 μ m
Pixel area	22.75 μ m ²	38.69 μ m ²	20.25 μ m ²
Distance	5.3m	6.2m	4.3m
Image pairs	1000	1000	1000

1) *System hardware*: Fig. 2 shows the controlled laboratory setting for the MIDPI data acquisition. We collect MIDPI training data by shooting natural images displayed on a 4K UHD (3840 \times 2160) HDR10 monitor by a digital camera. We obtain LR images with short focal lens and HR images with long focal lens. To prevent blur caused by possible vibrations of the camera, we mount the camera on a track dolly slider and trigger the shutter using a WiFi remote controller. Three cameras, Sony Nex-6, Canon 5D-MarkIII and Sony Alpha-a7RII, are used to increase the variety of camera statistics in reality.

2) *Setup of acquisition system*: To prevent possible moiré patterns in captured screen images, the camera should be placed at a sufficient distance from the monitor. We denote the focal length of the camera, the object distance and the pixel pitch of the screen by f , d and u_s respectively. The size of an imaged pixel on screen through the lens is

$$u_i = u_s \frac{f}{d} \quad (1)$$

Moiré patterns are caused by the interference between the screen image and the color filter array of the camera. By the Nyquist–Shannon sampling theorem, moiré patterns can be eliminated if the camera sensor sampling step size $u_c > 2u_i$. Then it follows from Eq. 1 that the moiré-free distance between the camera and the screen is

$$d > 2f \frac{u_s}{u_c} \quad (2)$$

As the focal length for capturing LR images is shorter than the focal length for HR images, eliminating moiré patterns in captured HR images will also ensure no moiré patterns in LR images. Therefore we determine the camera position by the long focal length for capturing HR images. In addition, to simplify the LR~HR registration, we set the focal plane (sensor array) of the camera parallel to the screen surface. To achieve this we display a square pattern on the screen, and make sure the pattern to remain a square in the captured screen image, by adjusting the universal angle plate on which the camera is mounted.

3) *Data collection process*: We conduct multiple shooting sessions using three cameras to ensure a sufficiently large data volume and diversity to facilitate deep learning. The camera specifications and settings for the data acquisition process are tabulated in Table I. To keep the consistency of each captured LR~HR image pair (X_i, \hat{Y}_i), we only change the focal length of the lens once for each camera. More specifically, We first capture all needed LR images with the same short focal length, then we adjust the focal length and capture the corresponding HR images. This can reduce the registration error caused by the frequent mechanical changes.

To remove all unnecessary variations among acquired images, all camera parameters irrelevant to spatial resolution, such as white balance, aperture size and exposure time, should be fixed. We thus collect raw Bayer images rather than JPEG images produced by the camera built-in image processing pipeline. The LR and HR raw Bayer images are demosaiced into corresponding RGB images of linear scale without any tone mapping nor gamma correction. We correct the lens distortion

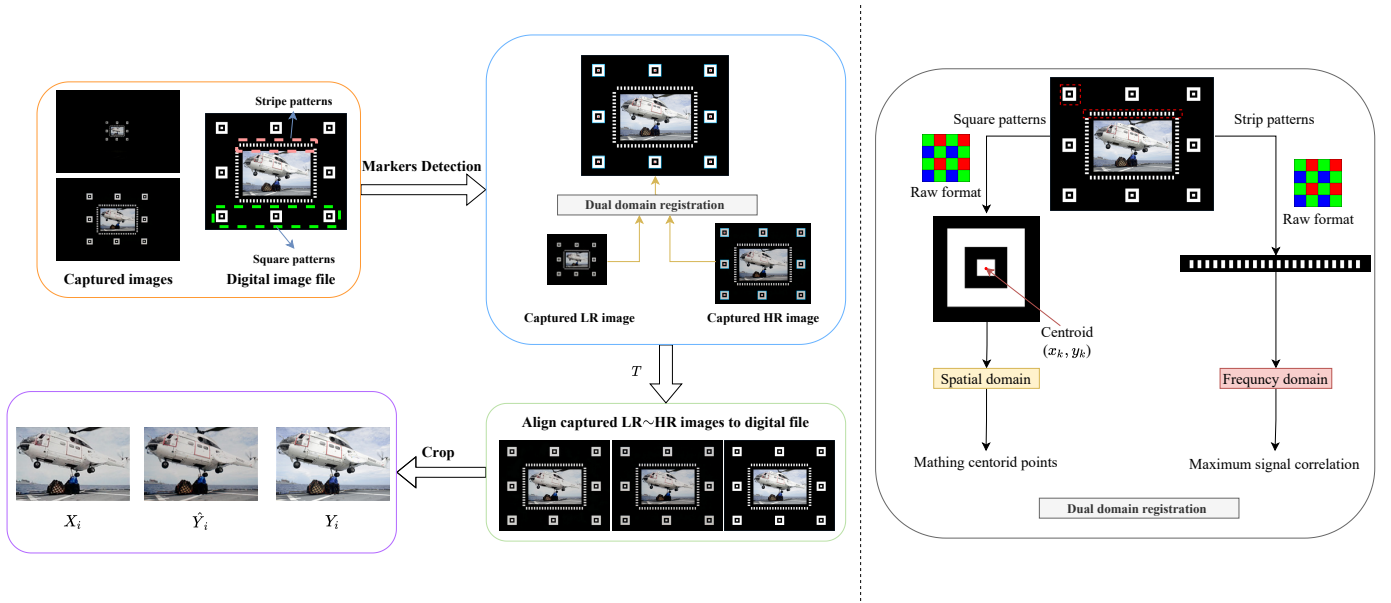


Fig. 4: Overall process of the image registration between the captured LR image X_i and the captured HR image \hat{Y}_i . The captured LR image X_i and the captured HR image \hat{Y}_i are aligned to the digital image Y_i .

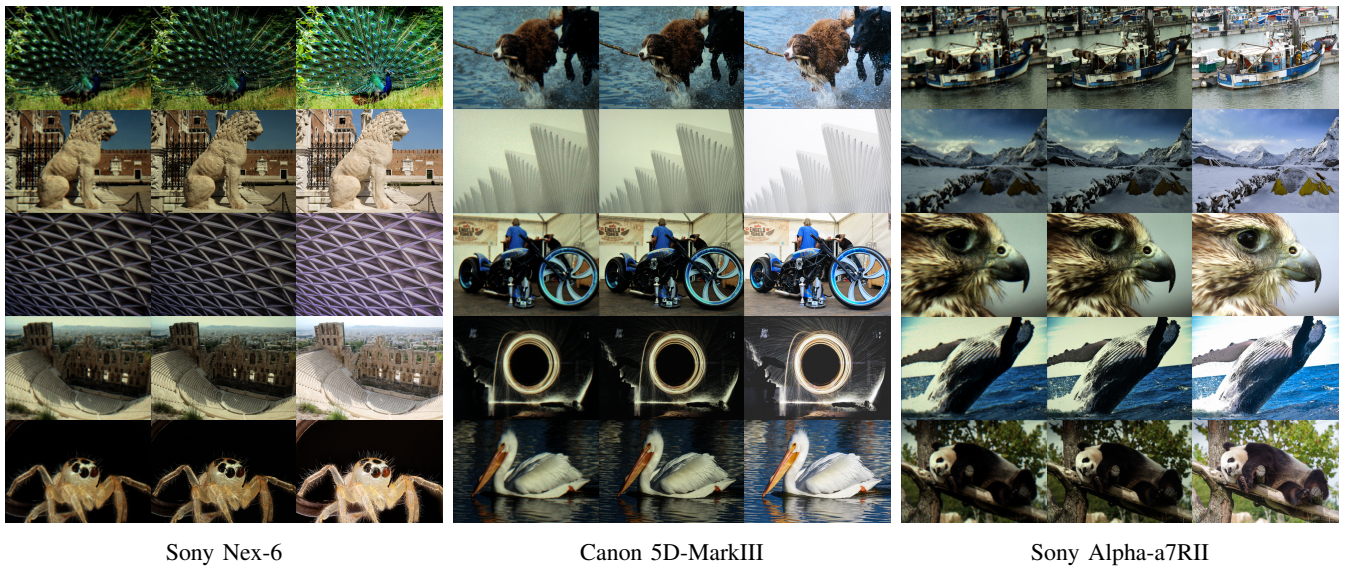


Fig. 5: Samples of the collected LR~HR image pairs in MIDPI. In each sample, the captured LR image X_i is placed on the left, the captured HR image \hat{Y}_i is placed on the middle and the digital HR image Y_i is placed on the right.

229 with Zhang’s method [42]. To factor out the influences of
 230 monitor backlight, we display a black image on the monitor
 231 at the beginning of every shooting process and subtract it
 232 from every captured image afterwards. The ultra-high quality
 233 monitor and the DSLR camera are remotely operated in a dark
 234 room so as to prevent any interference of ambient light and
 235 any motions of the monitor and camera.

236 As we argued in introduction section, the captured HR
 237 images \hat{Y}_i are not the exact ground truth images, which suffer
 238 from blur and noise when capturing the screen. During the
 239 dataset collection process, we simultaneously save the displayed
 240 high quality digital file Y_i .

B. LR~HR registration

241 Conventionally, keypoints based image registration algo-
 242 rithms, such as SIFT [41] and SURF [43], are used to align
 243 the LR images and HR images in real dataset collection [25],
 244 [27]. However, these general keypoints cannot achieve accurate
 245 pixel-wise registration, let alone sub-pixel level. Additionally,
 246 some parts of the real images cannot be aligned with the same
 247 homography matrix due to the disparity in depths. This problem
 248 often leads to noticeable perspective misalignment of LR~HR
 249 images captured in real scenes [26], [27]. Fig. 3 demonstrates
 250 such a perspective change caused by the different depths and
 251 distances. In the MIDPI system, the images are displayed
 252 on a flat monitor. Hence, the aforementioned misalignment
 253

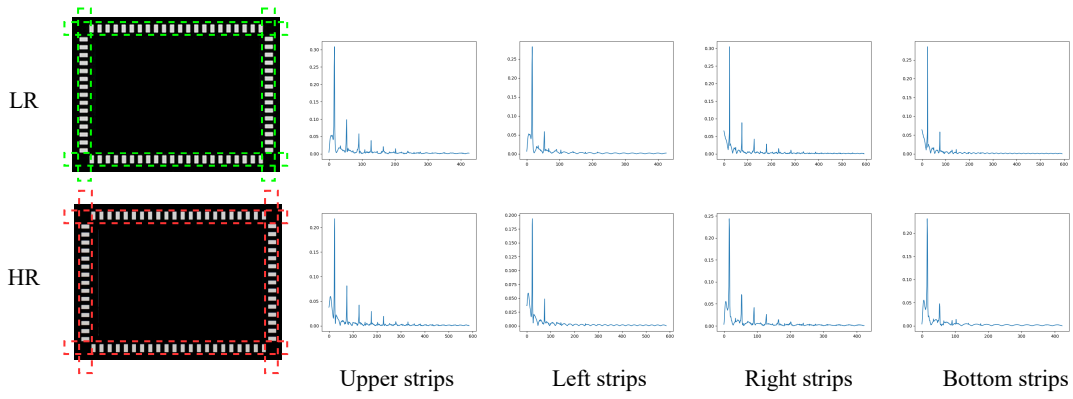


Fig. 6: Frequency spectrum of the stripe banners encircling the LR~HR images.

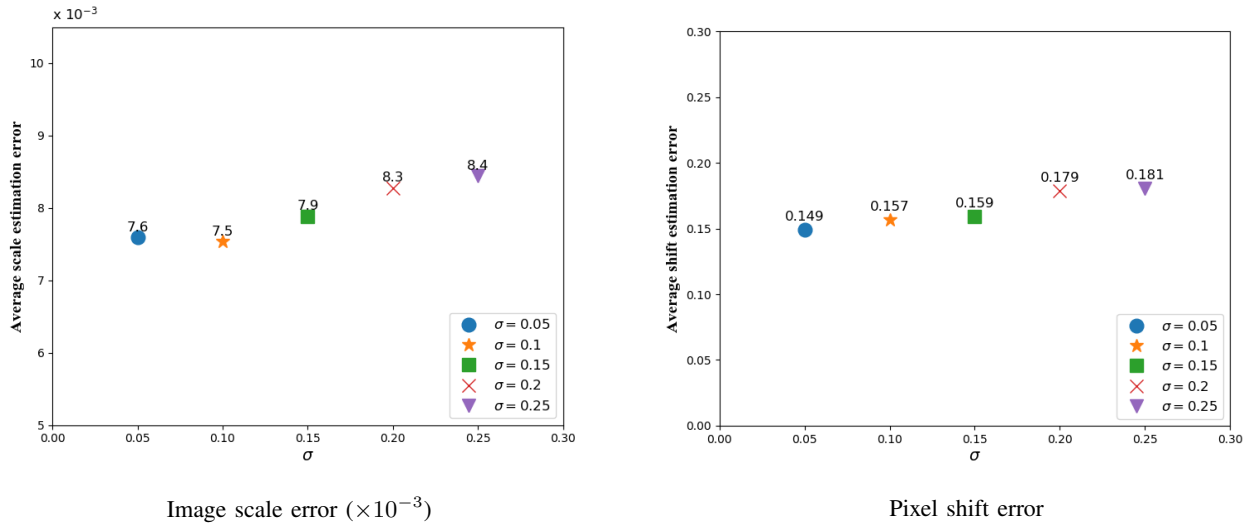


Fig. 7: Accuracy of the proposed image alignment algorithm in aligning randomly scaled and shifted images.

254 of captured realistic paired LR~HR images is inherently
 255 eliminated in the system.

256 To achieve robust and highly accurate LR~HR registration,
 257 we place special marks along the boundary of the image to
 258 be displayed on screen, as shown in Fig. 4. Two sets of
 259 markers are used to support a novel LR~HR registration
 260 method in dual spatial and frequency domains to be detailed
 261 in the next subsection. The first set consists of eight nested
 262 square patterns, four at the corners of the image, and the other
 263 four at the four sides of the image. These eight markers are
 264 for LR~HR registration in spatial domain. The second set
 265 consists of four bar patterns of a fixed frequency, two along
 266 the top and bottom image boundaries and two along the left
 267 and right image boundaries. These four bar patterns are used
 268 for LR~HR registration in frequency domain. Note that we
 269 match the patterns of raw Bayer format so as to achieve the
 270 better registration precision.

271 1) *Dual domain registration:* After the pre-calibration by
 272 making the camera parallel to the monitor surface, the trans-
 273 formation matrix between the LR~HR image pair is simplified to
 274 an affine transformation T . To register dual reference training
 275 data, we align both the captured LR image X_i and the captured

276 HR image \hat{Y}_i to the digital image file Y_i . To keep the training
 277 data same resolution, we upsample X_i and downsample Y_i to
 278 the size of \hat{Y}_i . Next, for simplicity, we introduce the registration
 279 process of (X_i, Y_i) , the same to (\hat{Y}_i, Y_i) . Fig 4 illustrates
 280 the overall registration process in MIDPI. We first detect all
 281 the nested square patterns and crop valid content regions of
 282 LR~HR. Then a centroid of each square pattern is calculated
 283 as a matching point for image alignment in spatial domain.
 284 The centroid is of sub-pixel accuracy and robust to align the
 285 LR~HR image pair regardless of the blur and noise of the
 286 images. Denote the detected area of k -th square pattern by Ω_k
 287 and the image moments $M_{ij} = \sum_x \sum_y x^i y^j \Omega_k(x, y)$, the k -th
 288 matching point of LR image $(x_k, y_k) = (\frac{M_{10}}{M_{00}}, \frac{M_{01}}{M_{00}})$. To match
 289 the corresponding centroid point (x'_k, y'_k) of the digital HR
 290 image, our method minimizes the following objective function
 291 with homogeneous coordinate representation:

$$\min_T \|TX - Y\|_2^2 \quad (3)$$

292 where X is a data matrix consisting of the eight centroid points
 293 (x_k, y_k) and Y is a counterpart data matrix of the centroid
 294 points (x'_k, y'_k) . We thus can get $T = YX^T(XX^T)^{-1}$.

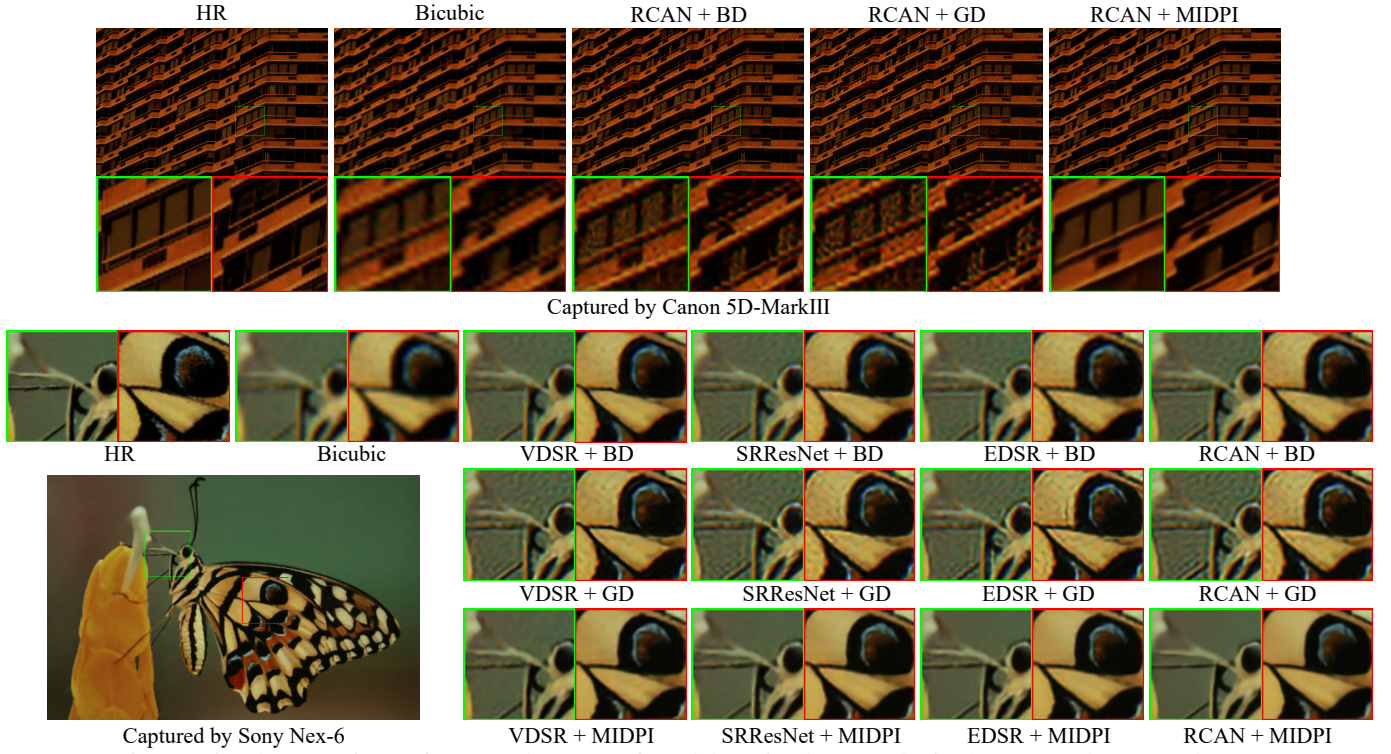


Fig. 8: Visual comparison of SR results ($\times 4$) of models trained on synthetic datasets and MIDPI dataset.

295 In addition, thanks to the purposefully designed patterns, where they have frequency spectra with distinctive peak frequencies, making it easy to maximize the signal correlation of the patterns to be matched, as demonstrated in Fig. 6. By matching the bar patterns in frequency domain, the image pair can achieve registration precision to within an arbitrary fraction of a pixel [44]. As the frequency resolution by FFT is limited *e.g.* 1 HZ interval, it is not precise enough to reach sub-pixel accuracy. Many prior works [45]–[47] solve it by locally searching the finer peak value. To detour this trouble, we maximize the cross-correlation [48] of the two patterns, which is equivalent to matching the spectra of the patterns. First, after aligning the captured LR image X_i to the digital image file Y_i , the four bar patterns can be located in the captured LR image X_i , as the bar positions are pre-set in the digital image file Y_i , of which the bar positions are fixed. We then can easily crop all the four bar patterns. Denote the cropped 2D bar signals (upper, bottom, left and right bars) of the image pair by (b_{X_m}, b_{Y_m}) , $m = 1, 2, 3, 4$, the zero mean normalized cross-correlation (ZNCC) between b_{X_m} and b_{Y_m} is:

$$\mathbf{r}_m(b_{X_m}, b_{Y_m}) = \left\langle \frac{b_{X_m} - \mathbb{E}(b_{X_m})}{\|b_{X_m} - \mathbb{E}(b_{X_m})\|}, \frac{b_{Y_m} - \mathbb{E}(b_{Y_m})}{\|b_{Y_m} - \mathbb{E}(b_{Y_m})\|} \right\rangle \quad (4)$$

315 where $\langle \cdot \rangle$ represents the inner product operation. If the peak frequency and phase of b_{X_m} faultlessly match the ones of b_{Y_m} , X_i and Y_i are perfectly aligned. In other words, the ZNCC score of b_{X_m} and b_{Y_m} should be maximized [49]. To this end, our algorithm minimizes the following objective function:

$$\min_T \sum_{m=1}^4 \|\mathbf{c} - \mathbf{r}_m(C_m(T \circ X_i), C_m(Y_i))\|_1 \quad (5)$$

320 where $\mathbf{r}_m(\cdot)$ denotes the ZNCC calculated by Eq. 4 and C_m represents a cropping operation which makes the aligned m -th bar pattern of X_i have the same size as the ones of Y_i , \circ is the affine transform operation. \mathbf{c} is a constant matrix. According to [50], the above objection w.r.t. T is nonlinear, which can be solved iteratively by a locally linear approximation that is

$$\min_{\Delta T} \sum_{m=1}^4 \|\mathbf{c} - \mathbf{r}_m(C_m(T \circ X_i), C_m(Y_i)) + \mathbf{J}_m \Delta T\|_1 \quad (6)$$

326 where \mathbf{J}_m is the Jacobian matrix of $-\mathbf{r}_m(C_m(T \circ X_i), C_m(Y_i))$ w.r.t. T , and this objective function can be solved by an iteratively reweighted least square method (IRLS) [51] as following:

$$\min_{\Delta T} \|\mathbf{w} \odot (\mathbf{J} - \mathbf{z})\|_2^2 \quad (7)$$

330 where $\mathbf{J} = \sum_{m=1}^4 \mathbf{J}_m \Delta T$ and \odot represents element-wise product, \mathbf{w} is the weight matrix and $\mathbf{z} = \mathbf{r}_m(C_m(T \circ X_i), C_m(Y_i)) - \mathbf{c}$. The solution of Eq. 7 is:

$$\Delta T = (\mathbf{J}^T \text{diag}(\mathbf{w})^2 \mathbf{J})^{-1} \mathbf{J}^T \text{diag}(\mathbf{w})^2 \mathbf{z} \quad (8)$$

333 then T can be updated by $T = T + \Delta T$. The iterative optimization process is summarized in Algorithm 1.

335 2) *Image color correction*: As there exists color shift of the monitor when capturing LR~HR image pairs (X_i, \hat{Y}_i) separately, it causes the color mismatching between the captured image pairs. This color mismatching would plague the CNN model training. To calibrate the color mismatching, we conduct a pixel-wise color calibration. Denote the image pixel value of \hat{Y}_i by $[R, G, B]_{in}$, the color calibration function is:

$$\Gamma([R, G, B]_{in}) = A \cdot [R, G, B]_{in} \quad (9)$$

Algorithm 1 Iterative Optimization Algorithm for T

Input: Maximum iteration n , error bound ϵ
 1: Initialize $T \leftarrow YX^T(XX^T)^{-1}$ by solving Eq. 3
 2: $iter \leftarrow 0$
 3: **while** $iter < n$ and $\Delta T < \epsilon$ **do**
 4: $\Delta T \leftarrow (\mathbf{J}^T \text{diag}(\mathbf{w})^2 \mathbf{J})^{-1} \mathbf{J}^T \text{diag}(\mathbf{w})^2 \mathbf{z}$ (Eq. 8)
 5: $T \leftarrow T + \Delta T$
 6: $iter \leftarrow iter + 1$
 7: **End while**
Output: T

343 where A is a 3×3 matrix corresponding to the color transfor-
 344 mation matrix. Our method minimizes the following objective
 345 function:

$$\min_A \left\| \Gamma(\hat{Y}_i) - X_i \right\|_2^2 \quad (10)$$

346 The color mismatching between the digital image file Y_i and the
 347 captured image is needless to correct, as the digital image file
 348 Y_i supervises the SR CNN models by its gradient information
 349 rather than pixel content. As shown in Fig. 5, it illustrates some
 350 samples of the aligned dual reference training data produced
 351 by our MIDPI system. In each sample, the captured LR image
 352 \hat{X}_i is placed on the left, the captured HR image \hat{Y}_i is placed
 353 on the middle and the digital HR image Y_i is placed on the
 354 right.

355 *C. Dual reference loss function*

356 In MIDPI system, except the camera captured HR images
 357 \hat{Y}_i , we have super high-quality reference images *i.e.* digital file
 358 Y_i . Compared to this digital file, the camera captured \hat{Y}_i may
 359 suffer from loss of high frequency features. This motivates
 360 us to supervise the SR model training by using both \hat{Y}_i and
 361 digital file Y_i . To this end, we proposed a dual reference loss
 362 function:

$$\mathcal{L}(\hat{X}_i, \hat{Y}_i, Y_i) = \left\| \hat{X}_i - \hat{Y}_i \right\|_1 + \lambda \left\| \nabla \hat{X}_i - \nabla Y_i \right\|_\infty \quad (11)$$

363 where \hat{X}_i is a prediction of a SR CNN model, ∇ is a differential
 364 operator and λ is a trade-off weight. The former ℓ_1 -norm
 365 term minimizes the pixel-wise error between the prediction \hat{X}_i
 366 and the captured HR image \hat{Y}_i . In addition, we introduce a
 367 regulation term to enforce the gradient similarity between the
 368 prediction \hat{X}_i and the digital HR image Y_i , improving the high
 369 frequency textures of the prediction \hat{X}_i . To avoid producing
 370 over-smooth results, we adopt an infinite norm. By minimizing
 371 the dual reference loss function $\mathcal{L}(\hat{X}_i, \hat{Y}_i, Y_i)$, the pixel PSF
 372 between X_i and \hat{Y}_i and the high frequency information of Y_i
 373 can be jointly learned by a SR CNN in an end-to-end manner.

374 **IV. EXPERIMENTAL RESULTS**

375 As reported in Table. I, to build the MIDPI datasets, we
 376 collect 3000 paired images from three DSLR cameras. For each
 377 MIDPI dataset (Sony Nex-6 MIDPI dataset, Canon 5D-MarkIII
 378 MIDPI dataset and Sony Alpha-a7RII MIDPI dataset), we
 379 randomly select one tenth of the number of image pairs to form
 380 test dataset, while using the rest of image pairs for training. In

this section, we use the Sony Nex-6 MIDPI dataset to examine
 the differences between models trained on synthetic datasets
 and the MIDPI dataset. Moreover, we are more interested in the
 performance and generalization of the MIDPI-trained model
 for real scenes. For this purpose, we conduct an evaluation of
 real scenes and all images of three MIDPI datasets are used for
 model training. Because of the various degradation produced
 by the camera lens and sensors, the MIDPI-trained models
 are not device-free. To measure this diffidence, we conduct a
 cross-camera test. Following previous work [12], [15], [17],
 quantitative metrics PSNR and SSIM are calculated on the Y
 channel in the YCbCr space.

In the training process, we randomly crop the training images
 into 256×256 patches to train all the models and the mini-batch
 size in all the experiments is set to 8. The trade-off weight λ
 is set 0.1. Adam optimizer [52] is chosen to train all models
 by setting initial learning rate 10^{-4} . The learning rate is fixed
 in first 10K iterations and linearly decay to 10^{-6} after 70K
 iterations. With same parameters setting, all the experiments
 are conducted on a PC with single NVIDIA TITAN XP GPU.

401 *A. Evaluation of proposed image alignment algorithm*

402 In this section, we evaluate the precision of the image pair
 403 registration algorithm in MIDPI system. In Fig. 7, we show an
 404 evaluation study of the image alignment algorithm proposed
 405 in Sec III-B. In this experiment, we prepare 1000 images with
 406 the stripe banners. For each of the image, we first resize it
 407 by a random scale factor between 0.98 to 1.02, then shift
 408 it randomly in both horizontal and vertical directions by -
 409 5~5 pixels. Please note that the shift amount is not necessarily
 410 integer. The resulting resampled image is added with zero mean
 411 Gaussian noise of standard deviation σ and fed to the proposed
 412 alignment algorithm. As plotted in Fig. 7, the estimated shift of
 413 the image is off by less than 0.2 pixel distance on average in
 414 comparison with the ground truth; and the error of the estimated
 415 scale is also negligible. Moreover, the added noise does not
 416 significantly affect the accuracy of the alignment algorithm.

417 *B. Results of laboratory datasets*

418 The ultimate criterion of success for the proposed MIDPI
 419 data collection procedure is whether the MIDPI-trained DCNN
 420 model for super resolution can indeed outperform the counter-
 421 part trained by other LR~HR datasets when both being applied
 422 to infer on real world images. But for the sake of completeness
 423 and reference purpose, let us first evaluate the inference results
 424 on MIDPI data. We compare how a given DCNN SR model
 425 performs when it is trained by different datasets, including both
 426 synthesized and MIDPI. In the comparison study, two synthetic
 427 LR~HR datasets, denoted by BD and GD, are generated by
 428 downsampling the captured HR images of the MIDPI dataset
 429 using bicubic and Gaussian kernels. Table. II reports the PSNR
 430 and SSIM values (with scaling factor $\times 4$) of different SR
 431 models VDSR [20], SRResNet [22], EDSR [15], RCAN [17]
 432 after trained by different datasets.

433 As reported in Table. II, for each of the five tested SR
 434 methods, the MIDPI-trained model has significant improvement
 435 over the BD-trained model and GD-trained model, with

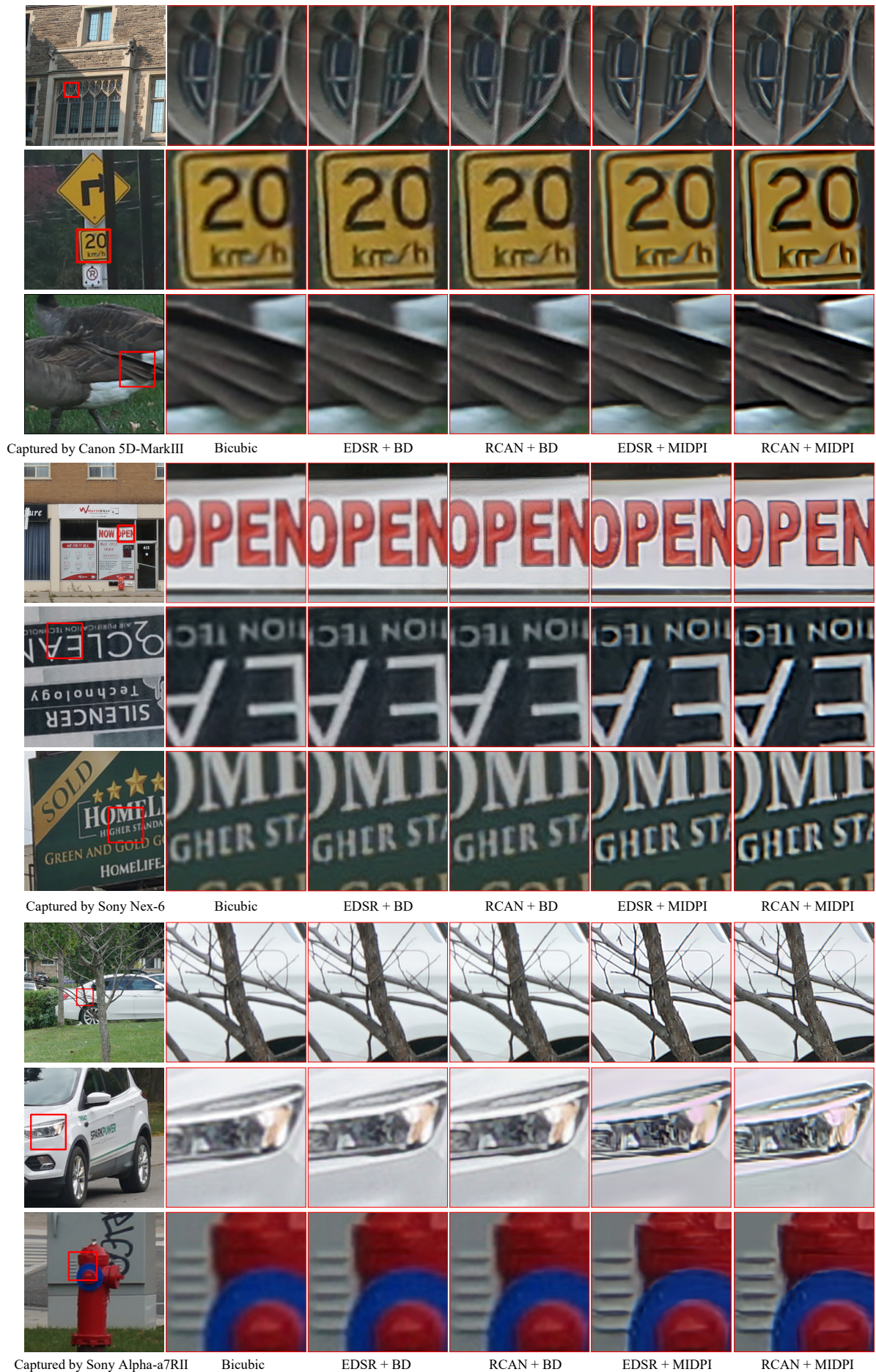


Fig. 9: SR results ($\times 4$) of real-world images outside our dataset. Zoom in for better view.

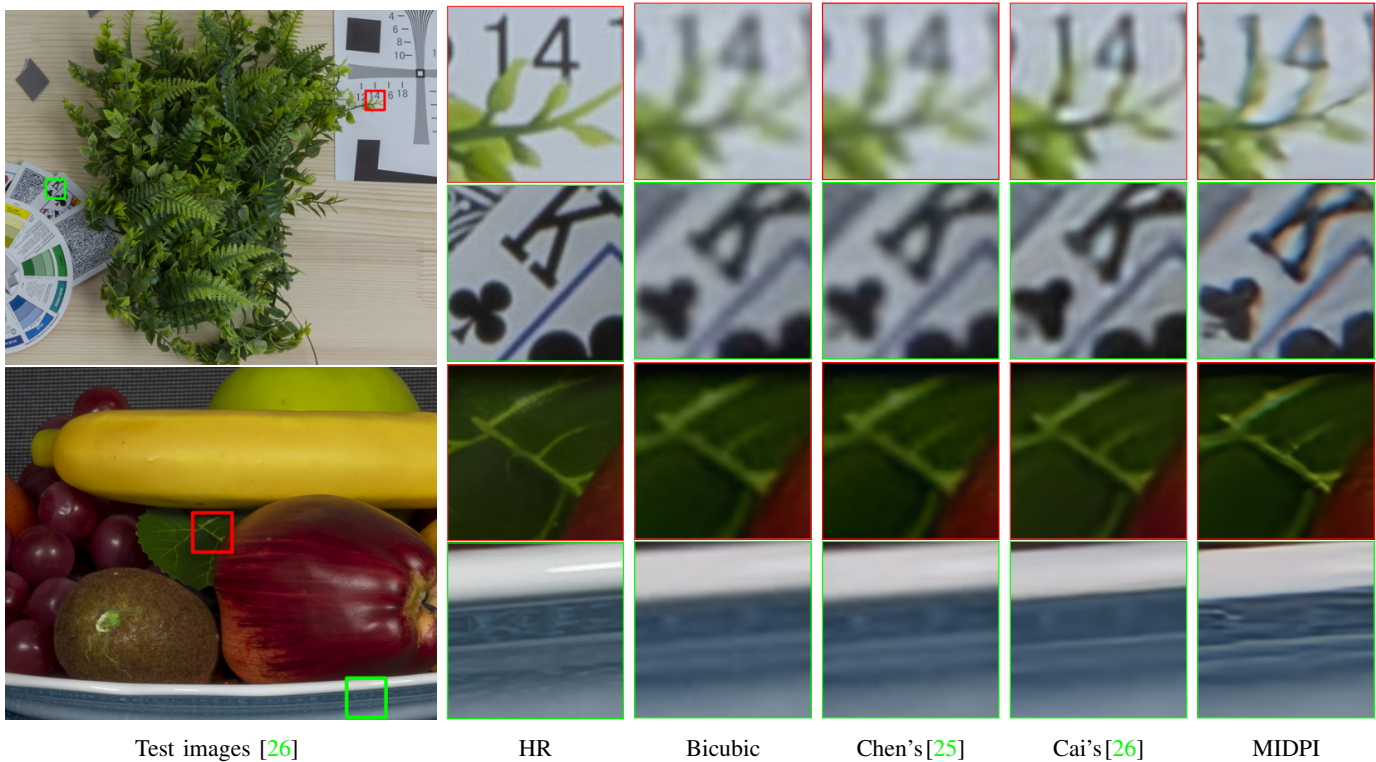


Fig. 10: SR results ($\times 4$) of real-world images from Cai's [26]. All models are of RCAN structure.

TABLE II: The comparison of different state-of-the-art methods trained on the synthetic datasets and the MIDPI dataset.

Methods ($\times 4$)	BD		GD		MIDPI	
	PSNR	SSIM	PSNR	SSIM	PSNR	SSIM
Bicubic	29.26	0.811	29.26	0.811	29.26	0.811
VDSR	30.41	0.838	30.64	0.841	32.12	0.860
SRResNet	30.51	0.837	30.59	0.836	32.53	0.871
EDSR	30.68	0.838	30.65	0.838	32.57	0.871
RCAN	30.78	0.842	30.71	0.839	33.15	0.877

gains from 1.7dB to 2.5dB. The visual quality comparison is presented in Fig. 8. As shown, the SR results associated with the training datasets BD and GD have more artifacts and more blurred edges than with the MIDPI dataset. It is expected that our MIDPI dataset outperforms BD and GD, because it characterizes statistical relations between the LR and HR images more accurately for the camera.

C. Results of superresolving real world images

Our MIDPI training dataset distinguishes itself from previous camera-acquired training datasets (e.g. [27]) for the SR task in that it has much higher sub-pixel precision of LR~HR registration and an extra high quality reference for model training. These advantages contribute to superior performance of MIDPI-trained DCNN models when the inference is carried out on screen images in the MIDPI dataset. A tantalizing question is whether the MIDPI-trained model can still keep its competitive edge when being applied to real world images. After all, images displayed on monitor are not the same as those captured in real world. Can the higher registration precision

of screen-displayed LR and HR image pairs more than offset the nuance differences between the screen-displayed and real world images?

To answer the above question, now we compare how a given DCNN SR model can superresolve real LR images, if trained by the MIDPI dataset versus if trained by other competing datasets. We choose two DCNN SR models (EDSR and RCAN) in the comparison study, because they are the two best performers in Table. II. Since for real LR images there are no ground truth images, we cannot compute PSNR and SSIM. Instead, we compare in Fig. 9 the output images of EDSR and RCAN after the networks are trained by the MIDPI dataset versus trained by the BD dataset. As shown, for real images captured by three different cameras, both MIDPI-trained EDSR and MIDPI-trained RCAN reproduce sharper edges and details than the models trained on synthesized datasets. This provides empirical evidence for the generalization capability of the MIDPI datasets from screen to real world images.

In the previous experiment of Fig. 9, the realistic images for inference and the training images are captured by the same DSLR cameras. Next we check what if the inference images and training images are captured by different cameras. We add in the comparison of Chen *et al.*'s dataset [25] and Cai *et al.*'s camera-captured SR training dataset [26], and retrain the RCAN models by the LR~HR images ($\times 4$) of these datasets. In Chen *et al.*'s dataset, similar to our MIDPI, the realistic LR~HR image pairs are collected under a controllable experimental environment. They printed 100 postcards and captured them twice with lenses of different focal lengths. Their image pairs are aligned by only using SIFT features.



Fig. 11: SR results ($\times 4$) of real-world images captured by iPhone 7plus and iPhone 11.

485 Cai *et al.*'s [26] collected LR~HR image pairs by capturing
 486 real-world static scenes.

487 In Fig.10, the test LR images are from Cai's dataset [26].
 488 The SR results are produced by three RCAN models trained
 489 by Chen's dataset, Cai's dataset and MIDPI dataset separately.
 490 As this figure shows, MIDPI trained model outperforms the
 491 competitors by achieving sharper edges. In contrast, Chen's
 492 dataset [25] and Cai's dataset [26] perform badly as they
 493 cannot register the image pairs precisely and lack an additional
 494 reference which provides high frequency information. Fig. 11

presents the SR inference results on images of the two
 495 smartphone cameras (iPhone 7plus and iPhone 11). The four
 496 RCAN models are trained by BD dataset, Chen's dataset
 497 [25], Cai's training dataset [26] and MIDPI, respectively.
 498 The experimental results show that the MIDPI-trained SR
 499 model recovers sharper and cleaner details with less artifacts
 500 than the other three models, when they are applied to novel
 501 cameras whose images are unseen during the training. All
 502 these test images are outside of our MIDPI-trained dataset.
 503 These experiments offer additional empirical evidence for the
 504

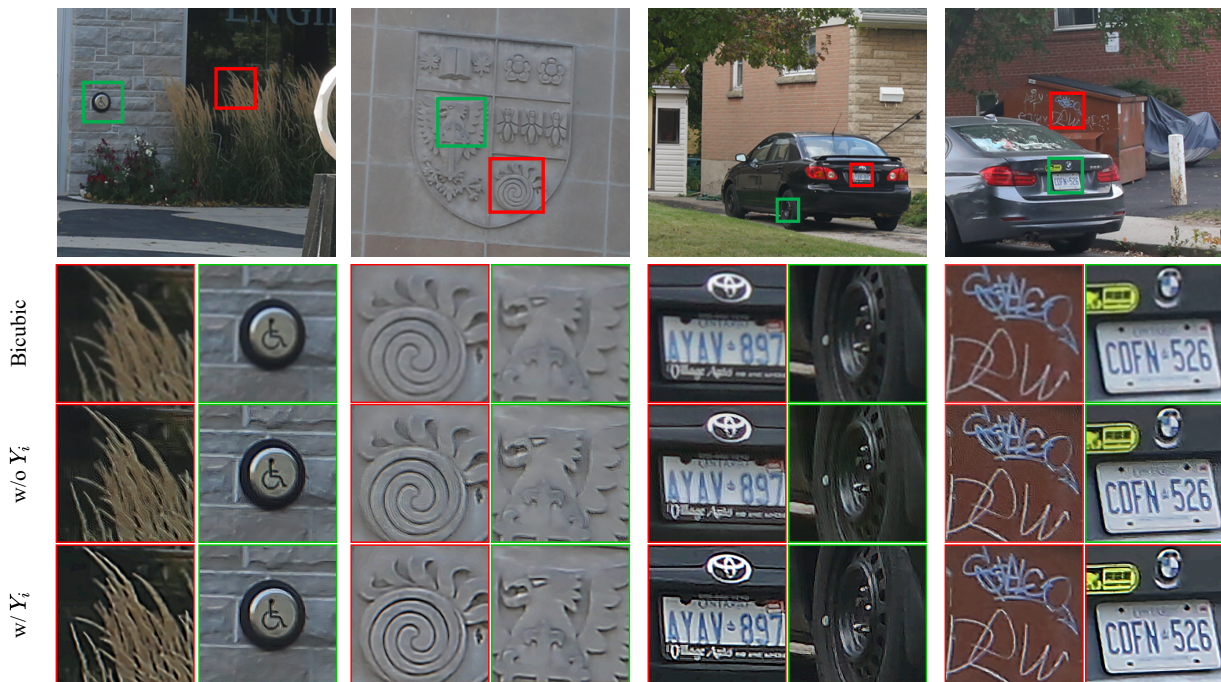


Fig. 12: Comparison of SR results with and without digital HR images for supervision. Zoom in for better view.

505 robustness of the MIDPI training data generation strategy.

506 *D. Ablation study of digital files*

507 To verify the advantages of the strategy by training SR
 508 models with digital HR images, we compare RACN models
 509 trained on the proposed MIDPI dataset w/ and w/o the digital
 510 HR reference Y_i . As shown in Fig. 12, the results of the model
 511 without Y_i have some wierd high-frequency artifacts around
 512 the edges. In contrast, the digital HR images trained model
 513 can produce clear results meanwhile erasing the unintended
 514 high-frequency blemishes. These improvement demonstrates the
 515 effectiveness of our propsoed dual reference for SR model
 516 training. With the dual reference strategy, the unintended
 517 artifacts of captured image pairs can be restrained, while the
 518 super high quality reference can promote the performance of
 519 the trained SR models.

520 *E. Cross-camera evaluation*

521 CNN methods are very sensitive to nuance differences
 522 between the training and inference data. Therefore, a CNN SR
 523 method will suffer performance losses if it is trained by images
 524 taken by one camera but is used to restore images taken by
 525 another. To evaluate the immunity of such performance losses,
 526 we conduct the following cross-camera experiments. We train
 527 three RCAN models by three camera-specific MIDPI datasets
 528 respectively, and then test them on images drawn from all the
 529 three MIDPI datasets that are unseen in the training. Table. III
 530 reports the PSNR and SSIM values of the experimental results.
 531 An interesting observation is that the performance decays
 532 between two different cameras, as shown in the first row of
 533 the Table. III, even if they are made by the same manufacturer
 534 (0.37 dB gap between Sony Nex-6 and Sony Alpha-a7RII).

TABLE III: Average PSNR/SSIM ($\times 4$) for cross-camera evaluation. All models are of RCAN structure.

Camera	Sony Nex-6	Canon 5D-MarkIII	Sony Alpha-a7RII
Sony Nex-6	33.15/0.877	32.55/0.809	32.78/0.893
Canon 5D-MarkIII	31.71/0.862	33.24/0.853	31.90/0.872
Sony Alpha-a7RII	32.14/0.868	32.17/0.801	33.21/0.903

535 Moreover, the performance gap between two cameras from
 536 different manufacturer is bigger (e.g., 0.60 dB gap between
 537 Sony Nex-6 and Canon 5D-MarkIII). As illustrated in the
 538 last row of the Table. III, both models trained by Sony Nex-
 539 6 MIDPI dataset and Canon 5D-MarkIII MIDPI dataset are
 540 not nearly as good as the Sony Alpha-a7RII MIDPI trained
 541 model. These observations suggest that for best performance
 542 the DCNN SR model trained by images captured by a camera
 543 should be applied to images of the same camera. Thanks to
 544 the high data collection throughput of the MIDPI system, Our
 545 MIDPI system can be easily employed to collect a mass of
 546 realistic SR image pairs. In out experiment, it only takes 6
 547 hours (500 image pairs per hour) to collect 3000 image pairs
 548 for three cameras. The size of MIDPI dataset is much larger
 549 than existing realistic SR datasets. With the proposed MIDPI
 550 system, one can simply collect training datasets for each of
 551 the intended cameras and build a camera-specific DCNN SR
 552 model for it.

553 **V. CONCLUSION**

554 The proposed MIDPI generation of training data for deep
 555 learning based superresolution offers unprecedented alignment
 556 accuracy between LR and HR image pairs captured by a camera.
 557 This unique advantage contributes to superior performance
 558 of MIDPI-trained DCNN SR models over the same models
 559 trained by other LR~HR datasets. In addition, MIDPI system

can collect sufficient paired data under lab conditions. It makes it easy to deploy specific SR models for any type of digital camera and real scene. The proposed unprecedented idea by using dual reference for training SR models, breaking through limitation of the used camera for realistic SR data collection. Our abundant experiments reveal the great effectiveness of our MIDPI dataset for CNN super-resolution models.

REFERENCES

- [1] W. T. Freeman, E. C. Pasztor, and O. T. Carmichael, "Learning low-level vision," *International journal of computer vision*, vol. 40, no. 1, pp. 25–47, 2000. **1**
- [2] R. Timofte, V. De, and L. V. Gool, "Anchored neighborhood regression for fast example-based super-resolution," in *2013 IEEE International Conference on Computer Vision*, 2013, pp. 1920–1927. **1**
- [3] G. Freedman and R. Fattal, "Image and video upscaling from local self-examples," *ACM Trans. Graph.*, vol. 28, no. 3, pp. 1–10, 2010. **1**
- [4] D. Glasner, S. Bagon, and M. Irani, "Super-resolution from a single image," in *2009 IEEE 12th International Conference on Computer Vision*, 2009, pp. 349–356. **1**
- [5] J. Yang, Z. Lin, and S. Cohen, "Fast image super-resolution based on in-place example regression," in *2013 IEEE Conference on Computer Vision and Pattern Recognition*, 2013, pp. 1059–1066. **1**
- [6] J.-B. Huang, A. Singh, and N. Ahuja, "Single image super-resolution from transformed self-exemplars," in *Proceedings of the IEEE conference on computer vision and pattern recognition*, 2015, pp. 5197–5206. **1, 2**
- [7] J. Yang, J. Wright, T. S. Huang, and Y. Ma, "Image super-resolution via sparse representation," *IEEE transactions on image processing*, vol. 19, no. 11, pp. 2861–2873, 2010. **1**
- [8] C. Dong, C. C. Loy, K. He, and X. Tang, "Image super-resolution using deep convolutional networks," *IEEE transactions on pattern analysis and machine intelligence*, vol. 38, no. 2, pp. 295–307, 2015. **1**
- [9] C. Ledig, L. Theis, F. Huszár, J. Caballero, A. Cunningham, A. Acosta, A. Aitken, A. Tejani, J. Totz, Z. Wang *et al.*, "Photo-realistic single image super-resolution using a generative adversarial network," in *Proceedings of the IEEE conference on computer vision and pattern recognition*, 2017, pp. 4681–4690. **1**
- [10] Y. Zhang, K. Li, K. Li, L. Wang, B. Zhong, and Y. Fu, "Image super-resolution using very deep residual channel attention networks," in *Proceedings of the European Conference on Computer Vision (ECCV)*, 2018, pp. 286–301. **1**
- [11] Y. Blau, R. Mechrez, R. Timofte, T. Michaeli, and L. Zelnik-Manor, "The 2018 pirm challenge on perceptual image super-resolution," in *Proceedings of the European Conference on Computer Vision (ECCV)*, 2018, pp. 0–0. **1**
- [12] R. Timofte, S. Gu, J. Wu, and L. Van Gool, "Ntire 2018 challenge on single image super-resolution: Methods and results," in *Proceedings of the IEEE conference on computer vision and pattern recognition workshops*, 2018, pp. 852–863. **1, 7**
- [13] C. Dong, C. C. Loy, K. He, and X. Tang, "Image super-resolution using deep convolutional networks," *IEEE transactions on pattern analysis and machine intelligence*, vol. 38, no. 2, pp. 295–307, 2015. **1**
- [14] W. Shi, J. Caballero, F. Huszár, J. Totz, A. Aitken, R. Bishop, D. Rueckert, and Z. Wang, "Real-time single image and video super-resolution using an efficient sub-pixel convolutional neural network," 06 2016. **1**
- [15] B. Lim, S. Son, H. Kim, S. Nah, and K. Mu Lee, "Enhanced deep residual networks for single image super-resolution," in *Proceedings of the IEEE conference on computer vision and pattern recognition workshops*, 2017, pp. 136–144. **1, 7**
- [16] Y. Zhang, Y. Tian, Y. Kong, B. Zhong, and Y. Fu, "Residual dense network for image super-resolution," in *Proceedings of the IEEE conference on computer vision and pattern recognition*, 2018, pp. 2472–2481. **1**
- [17] Y. Zhang, K. Li, K. Li, L. Wang, B. Zhong, and Y. Fu, "Image super-resolution using very deep residual channel attention networks," in *Proceedings of the European Conference on Computer Vision (ECCV)*, 2018, pp. 286–301. **1, 7**
- [18] F. Yang, H. Yang, J. Fu, H. Lu, and B. Guo, "Learning texture transformer network for image super-resolution," in *Proceedings of the IEEE/CVF Conference on Computer Vision and Pattern Recognition*, 2020, pp. 5791–5800. **1**
- [19] J. Kim, J. K. Lee, and K. M. Lee, "Deeply-recursive convolutional network for image super-resolution," in *2016 IEEE Conference on Computer Vision and Pattern Recognition (CVPR)*, 2016, pp. 1637–1645. **1**
- [20] J. Kim, J. Kwon Lee, and K. Mu Lee, "Accurate image super-resolution using very deep convolutional networks," in *Proceedings of the IEEE conference on computer vision and pattern recognition*, 2016, pp. 1646–1654. **1, 7**
- [21] J. Johnson, A. Alahi, and L. Fei-Fei, "Perceptual losses for real-time style transfer and super-resolution," in *European conference on computer vision*. Springer, 2016, pp. 694–711. **1**
- [22] C. Ledig, L. Theis, F. Huszár, J. Caballero, A. Cunningham, A. Acosta, A. Aitken, A. Tejani, J. Totz, Z. Wang *et al.*, "Photo-realistic single image super-resolution using a generative adversarial network," in *Proceedings of the IEEE conference on computer vision and pattern recognition*, 2017, pp. 4681–4690. **1, 7**
- [23] M. S. Sajjadi, B. Scholkopf, and M. Hirsch, "Enhancenet: Single image super-resolution through automated texture synthesis," in *Proceedings of the IEEE International Conference on Computer Vision*, 2017, pp. 4491–4500. **1**
- [24] X. Wang, K. Yu, S. Wu, J. Gu, Y. Liu, C. Dong, Y. Qiao, and C. Change Loy, "Esrgan: Enhanced super-resolution generative adversarial networks," in *Proceedings of the European Conference on Computer Vision (ECCV) Workshops*, September 2018. **1**
- [25] C. Chen, Z. Xiong, X. Tian, Z.-J. Zha, and F. Wu, "Camera lens super-resolution," 2019. **1, 2, 4, 9, 10**
- [26] J. Cai, H. Zeng, H. Yong, Z. Cao, and L. Zhang, "Toward real-world single image super-resolution: A new benchmark and a new model," in *Proceedings of the IEEE International Conference on Computer Vision*, 2019. **1, 2, 3, 4, 9, 10**
- [27] X. C. Zhang, Q. Chen, R. Ng, and V. Koltun, "Zoom to learn, learn to zoom," 2019. **1, 2, 4, 9**
- [28] M. Bevilacqua, A. Roumy, C. Guillemot, and M. L. Alberi-Morel, "Low-complexity single-image super-resolution based on nonnegative neighbor embedding," 2012. **2**
- [29] E. M. Zeyde Roman and P. Matan, "On single image scale-up using sparse-representations," in *International conference on curves and surfaces*. Springer, 2010, pp. 711–730. **2**
- [30] R. Timofte, E. Agustsson, L. Van Gool, M.-H. Yang, and L. Zhang, "Ntire 2017 challenge on single image super-resolution: Methods and results," in *Proceedings of the IEEE conference on computer vision and pattern recognition workshops*, 2017, pp. 114–125. **2**
- [31] W. Dong, L. Zhang, G. Shi, and X. Li, "Nonlocally centralized sparse representation for image restoration," *IEEE transactions on Image Processing*, vol. 22, no. 4, pp. 1620–1630, 2012. **2**
- [32] X. Xu, Y. Ma, and W. Sun, "Towards real scene super-resolution with raw images," *2019 IEEE/CVF Conference on Computer Vision and Pattern Recognition (CVPR)*, pp. 1723–1731, 2019. **2**
- [33] J. Yoo, N. Ahn, and K.-A. Sohn, "Rethinking data augmentation for image super-resolution: A comprehensive analysis and a new strategy," 04 2020. **2**
- [34] D. S. Jeon, S.-H. Baek, I. Choi, and M. H. Kim, "Enhancing the spatial resolution of stereo images using a parallax prior," in *Proceedings of the IEEE Conference on Computer Vision and Pattern Recognition*, 2018, pp. 1721–1730. **2**
- [35] L. Wang, Y. Wang, Z. Liang, Z. Lin, J. Yang, W. An, and Y. Guo, "Learning parallax attention for stereo image super-resolution," in *Proceedings of the IEEE Conference on Computer Vision and Pattern Recognition*, 2019, pp. 12250–12259. **2**
- [36] M. Fritsche, S. Gu, and R. Timofte, "Frequency separation for real-world super-resolution," 10 2019, pp. 3599–3608. **2**
- [37] Y. Yuan, S. Liu, J. Zhang, Y. Zhang, C. Dong, and L. Lin, "Unsupervised image super-resolution using cycle-in-cycle generative adversarial networks," in *Proceedings of the IEEE Conference on Computer Vision and Pattern Recognition Workshops*, 2018, pp. 701–710. **2**
- [38] A. Bulat, J. Yang, and G. Tzimiropoulos, "To learn image super-resolution, use a gan to learn how to do image degradation first," in *Computer Vision – ECCV 2018*. Cham: Springer International Publishing, 2018, pp. 187–202. **2**
- [39] C. Qu, D. Luo, E. Monari, T. Schuchert, and J. Beyerer, "Capturing ground truth super-resolution data," in *2016 IEEE International Conference on Image Processing (ICIP)*, 2016, pp. 2812–2816. **2**
- [40] T. Köhler, M. Bätz, F. Naderi, A. Kaup, A. Maier, and C. Riess, "Toward bridging the simulated-to-real gap: Benchmarking super-resolution on real data," *IEEE Transactions on Pattern Analysis and Machine Intelligence*, vol. 42, no. 11, pp. 2944–2959, 2020. **2**
- [41] D. G. Lowe, "Distinctive image features from scale-invariant keypoints," *International journal of computer vision*, vol. 60, no. 2, pp. 91–110, 2004. **2, 4**

- 708 [42] Z. Zhang, “A flexible new technique for camera calibration,” *IEEE*
709 *Transactions on pattern analysis and machine intelligence*, vol. 22, no. 11,
710 pp. 1330–1334, 2000. 4
- 711 [43] H. Bay, T. Tuytelaars, and L. Van Gool, “Surf: Speeded up robust
712 features,” in *European conference on computer vision*. Springer, 2006,
713 pp. 404–417. 4
- 714 [44] M. Guizar-Sicairos, S. Thurman, and J. Fienup, “Efficient subpixel image
715 registration algorithms,” *Optics letters*, vol. 33, pp. 156–8, 02 2008. 6
- 716 [45] H. S. Stone, M. T. Orchard, E.-C. Chang, and S. A. Martucci, “A fast
717 direct fourier-based algorithm for subpixel registration of images,” *IEEE*
718 *Transactions on geoscience and remote sensing*, vol. 39, no. 10, pp.
719 2235–2243, 2001. 6
- 720 [46] H. Foroosh, J. B. Zerubia, and M. Berthod, “Extension of phase correla-
721 tion to subpixel registration,” *IEEE transactions on image processing*,
722 vol. 11, no. 3, pp. 188–200, 2002. 6
- 723 [47] Wikipedia contributors, “Phase correlation — wikipedia, the free
724 encyclopedia.” 2021, [Online; accessed 22-June-2021]. [Online].
725 Available: https://en.wikipedia.org/wiki/Phase_correlation 6
- 726 [48] Wikipedia contributors, “Cross-correlation — wikipedia, the free
727 encyclopedia.” 2021, [Online; accessed 22-June-2021]. [Online].
728 Available: <https://en.wikipedia.org/wiki/Cross-correlation> 6
- 729 [49] L. Di Stefano, S. Mattoccia, and F. Tombari, “Zncc-based template
730 matching using bounded partial correlation,” *Pattern recognition letters*,
731 vol. 26, no. 14, pp. 2129–2134, 2005. 6
- 732 [50] J. Odobez and P. Bouthemy, “Robust multiresolution estimation of
733 parametric motion models,” *Journal of Visual Communication and Image*
734 *Representation*, vol. 6, no. 4, pp. 348–365, 1995. [Online]. Available:
735 <https://www.sciencedirect.com/science/article/pii/S1047320385710292> 6
- 736 [51] R. Chartrand and W. Yin, “Iteratively reweighted algorithms for com-
737 pressive sensing,” 05 2008, pp. 3869 – 3872. 6
- 738 [52] D. P. Kingma and J. Ba, “Adam: A method for stochastic optimization,”
739 *arXiv preprint arXiv:1412.6980*, 2014. 7